Journal of ELECTRONIC MATERIALS, Vol. 46, No. 1, 2017
DOI: 10.1007/s11664-016-4876-8

Electrochemical Performance of Morphologically Different Bi_2WO_6 Nanostructures Synthesized via a Hydrothermal Route

FEI WANG,[1] HUA YANG,[1,2] HAIMIN ZHANG,[1] JUNYAN SU,[1] and XIANGXIAN WANG[1]

1.—School of Science, Lanzhou University of Technology, Lanzhou 730050, China. 2.—e-mail: hyang@lut.cn

Morphologically different Bi_2WO_6 nanostructures have been synthesized via a hydrothermal route, where the morphology was tailored by varying the pH value of the precursor solution. The samples prepared at pH 1, 7, and 11 consisted of flower-like hierarchical structures with average diameter of 7 μm, irregular flake-like structures with average thickness of 90 nm, and uniform spherical structures with average size of 85 nm, respectively. The electrochemical performance of the as-prepared Bi_2WO_6 samples was investigated by cyclic voltammetry, galvanostatic charge–discharge measurements, and electrochemical impedance spectroscopy. In 1 M KOH electrolyte at current density of 0.5 mA cm^{-2}, the specific capacitance of the Bi_2WO_6 with flower-like hierarchical, flake-like, and spherical structure was measured to be 255 F g^{-1}, 214 F g^{-1}, and 412 F g^{-1}, respectively. After 850 charge–discharge cycles at current density of 3 mA cm^{-2}, the capacitance of the three samples remained at 87%, 78%, and 95% of the initial value, respectively. Among the three types of Bi_2WO_6 morphology, the spherical structure delivered the best electrochemical performance.

Key words: Bi_2WO_6 nanostructures, hydrothermal method, different morphologies, electrochemical performance

INTRODUCTION

With the rapid development of economy and society, the ever-increasing energy demands and depletion of nonrenewable fossil fuels have stimulated development of new energy sources as well as energy storage technologies. Supercapacitors, also known as electrochemical capacitors, have attracted a great deal of interest as unique electrical energy storage devices in recent years, bridging the gap between electrolytic capacitors and rechargeable batteries. They typically store 10–100 times the energy of electrolytic capacitors per unit volume or mass, and can accept and deliver charge much faster than batteries. Furthermore, supercapacitors can endure almost ten times the number of charge–discharge cycles of rechargeable batteries. These advantages make supercapacitors attractive for special applications such as consumer electronics, hybrid electric vehicles, memory backup systems, uninterruptible power supplies, etc.[1,2] According to their energy storage mechanism, supercapacitors are classified into electric double-layer capacitors and pseudocapacitors.[3,4] Electric double-layer capacitance arises due to physical accumulation of charges at electrode–electrolyte interfaces under the action of an electric field, while pseudocapacitance is associated with Faradaic electron charge transfer achieved by redox reactions, intercalation or electrosorption at the surface of the electrode material. Electric double-layer capacitors using carbon materials as the electrode generally deliver specific capacitance of 100 F g^{-1} to 350 F g^{-1}.[5,6] In comparison, metal-oxide-based pseudocapacitors can offer much higher capacitance and have been the focus of recent research. Examples of these metal oxides include RuO_2, MnO_2, Fe_2O_3, Co_3O_4, V_2O_5, NiO, Bi_2O_3, and CuO.[7–14] Among these, RuO_2

(Received June 3, 2016; accepted August 12, 2016; published online August 30, 2016)

has been considered as one of the most promising electrode materials since it can deliver high energy density and specific capacitance (1300 F g^{-1}) with excellent cycling stability.[7] However, commercial application of RuO_2 is restricted due to its high cost and toxicity.

Recently, bismuth tungstate (Bi_2WO_6) has been extensively studied as an outstanding functional material. This oxide has a special layered structure constructed by alternation of perovskite-like units $(WO_4)^{2-}$ and $(Bi_2O_2)^{2+}$ layers, and exhibits numerous interesting properties such as ferroelectricity, piezoelectricity, nonlinear dielectric susceptibility, gas sensitivity to alcohol, thermal conductivity, and photocatalytic activity.[15–21] Furthermore, Nithya et al. demonstrated that Bi_2WO_6 can be used as a promising electrode material for pseudosupercapacitors.[22] It is noted that an electrochemical reaction occurs at the surface of pseudocapacitive materials, and only a very thin layer of material can be involved in the charge storage process. This implies that the morphology and microstructure of a material have an important influence on its electrochemical performance; in particular, creation of nanostructures offers great potential to achieve excellent specific capacitance, since nanostructures can provide relatively short diffusion paths and high surface area. In this work, we comparatively investigated the electrochemical performance of morphologically different Bi_2WO_6 nanostructures including flower-like hierarchical structures, flake-like structures, and spherical structures, synthesized via a hydrothermal route.

EXPERIMENTAL PROCEDURES

Bi_2WO_6 nanostructures were synthesized via a hydrothermal route as described in literature.[23] $Bi(NO_3)_3{\cdot}5H_2O$ (0.002 mol) and $Na_2WO_4{\cdot}2H_2O$ (0.001 mol) were dissolved in 20 mL acetic acid solution and 20 mL distilled water, respectively. The two solutions were slowly mixed together under constant magnetic stirring. The mixture solution was adjusted to pH 1, 7 or 11 by adding NaOH solution, then made up to 70 mL by adding distilled water. The resultant solution was transferred to and sealed in a Teflon-lined stainless-steel autoclave of 100 mL capacity and submitted to hydrothermal treatment at 200°C. After reaction for 24 h, the autoclave was naturally cooled down to room temperature. The produced precipitate was collected and washed several times with distilled water and absolute ethanol, then dried in a thermostated drying oven at 60°C for 8 h to obtain the final Bi_2WO_6 products.

The phase purity of the as-prepared Bi_2WO_6 samples was examined by means of x-ray powder diffraction (XRD) analysis with Cu K_α radiation. Particle morphology was investigated by field-emission scanning electron microscopy (SEM).

The electrochemical performance of the Bi_2WO_6 samples was tested using a CST 350 electrochemical workstation with a three-electrode cell configuration, including a working electrode, counterelectrode, and reference electrode. Platinum foil served as the counterelectrode, and a standard calomel electrode (SCE) served as the reference electrode. The working electrode was prepared as follows: Bi_2WO_6, carbon black, and polyvinylidene fluoride (PVDF) were mixed at weight ratio of 8:1:1 using ethyl alcohol as solvent to form slurry. The slurry was uniformly coated onto a Ni foam electrode with area of 1 cm^2, which was dried at 60°C for 24 h in a thermostated drying oven. The mass of Bi_2WO_6 on the Ni foam electrode was 1 mg cm^{-2}. KOH aqueous solution with concentration of 1 mol L^{-1} (M) was used as electrolyte. The electrochemical performance of the Bi_2WO_6 samples was investigated by cyclic voltammetry (CV), electrochemical impedance spectroscopy (EIS), and galvanostatic charge–discharge measurements.

RESULTS AND DISCUSSION

Figure 1a, b, and c show SEM images of the Bi_2WO_6 samples prepared at pH 1, 7, and 11, respectively. The three samples are designated as S-pH1, S-pH7, and S-pH11, respectively. It is seen that different morphologies of Bi_2WO_6 were produced by varying the pH value of the reaction solution. The sample prepared at pH 1 consisted of flower-like hierarchical structures with average diameter of 7 μm (Fig. 1a). At pH 7, the resulting sample exhibited irregular flake-like structure with average thickness of about 90 nm (Fig. 1b). The SEM image in Fig. 1c reveals the synthesis of uniform spherical structures with average size of 85 nm at pH 11. Figure 1d shows the XRD patterns of the three Bi_2WO_6 samples. All diffraction peaks from the samples could be indexed to the orthorhombic Bi_2WO_6 phase (PDF card no. 73-2020), and no traces of other impurity phases were detected in the XRD patterns.

Figure 2 shows the CV curves of the Bi_2WO_6 samples, obtained at various scan rates ranging from 5 mV s^{-1} to 50 mV s^{-1} over the potential window between −1.0 V and 0 V. It is seen that, for the three morphologically different samples and at all scan rates, the CV curves present a sharp reduction peak R and two oxidation peaks O_1 and O_2, and furthermore the reduction and oxidation potentials undergo only a slight shift in negative and positive direction with increase in the scan rate, respectively. These CV curves imply a fast and reversible redox reaction and good pseudocapacitive behavior of the Bi_2WO_6. It is noted that the CV curves of Bi_2WO_6 are very similar to those of bismuth-based oxides such as Bi_2O_3, $BiPO_4$, $BiVO_4$, and $CuBi_2O_4$,[24–27] suggesting that the oxidation state of bismuth plays a vital role in the electrochemical mechanism. According to the redox

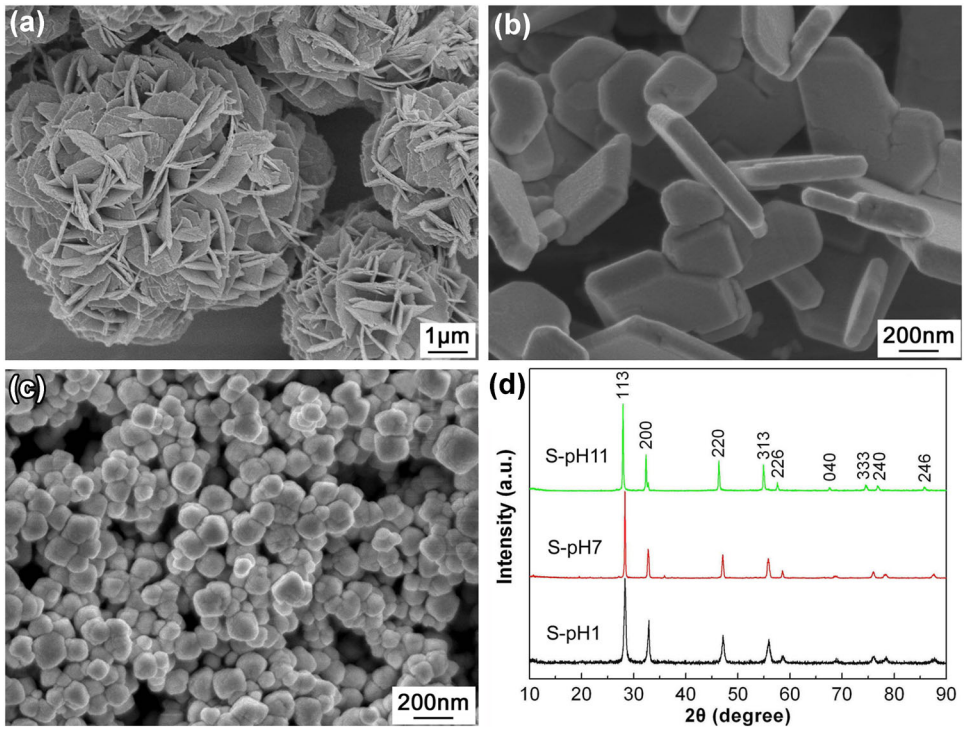

Fig. 1. SEM images of Bi_2WO_6 samples prepared at pH (a) 1, (b) 7, and (c) 11. (d) XRD patterns of Bi_2WO_6 samples prepared at pH 1, 7 and 11 (S-pH1, S-pH7, and S-pH11, respectively).

mechanism described by Vivier et al.,[28] the first step of the reduction process involves partial dissolution of Bi_2WO_6 to the ionic species BiO^{2-}. The reduction peak R arises from reduction of Bi(III) to Bi metal through the reaction pathway described by Eqs. 1, 2, and 3. The oxidation peaks O_1 and O_2 are due to oxidation of Bi metal to Bi(III), and the involved reaction process can be described by Eqs. 4, 5, 6, and 7.

$$BiO_2^- + e^- \rightarrow BiO_2^{2-} \tag{1}$$

$$2H_2O + 3BiO_2^{2-} \overset{\text{disproportionation}}{\longleftrightarrow} 2BiO_2^- + 4OH^- + Bi^0 \tag{2}$$

$$Bi^{(0)} \rightarrow Bi_{(metal)} \tag{3}$$

$$Bi_{(metal)} \rightarrow Bi^+ + e^- \tag{4}$$

$$3Bi^+ \overset{\text{disproportionation}}{\longleftrightarrow} Bi^{3+} + 2Bi_{(metal)} \tag{5}$$

$$3OH^- + Bi^{3+} \rightarrow Bi(OH)_3 \tag{6}$$

$$Bi(OH)_3 \rightarrow BiOOH + H_2O \tag{7}$$

The galvanostatic charge–discharge performance of the Bi_2WO_6 samples was investigated at various current densities ranging from 0.5 mA cm^{-2} to 5 mA cm^{-2} over the potential window between −1.0 V and 0 V. Figure 3a, b, and c show the charge–discharge curves for samples S-pH1, S-pH7, and S-pH11, respectively. It is seen that the charge–discharge curves for the three samples resemble each other quite closely. During the discharge process, the potential undergoes three stages, i.e., an initial sudden drop, followed by a plateau, and a final decrease. The initial sudden drop in the potential can possibly be ascribed to the solution resistance, the following potential plateau arises from the electrochemical reaction, and the final decrease in the potential is due to ion concentration polarization.[2] The nonlinear nature of the charge–discharge curves suggests that the electrochemical reaction takes place due to the redox mechanism, and this result is concordant with the CV results shown in Fig. 2. The specific capacitance (C) of the samples can be calculated using the equation

$$C = \frac{It}{m\Delta V}, \tag{8}$$

where C, I, t, m, and ΔV are the specific capacitance (F g^{-1}) of the sample, the discharging current (A), the discharging time (s), the mass of Bi_2WO_6 (g), and the discharging potential range (V), respectively. The specific capacitance values calculated for the Bi_2WO_6 samples at various current densities are shown in Fig. 3d. At current density of 0.5 mA cm^{-2}, the specific capacitance of samples

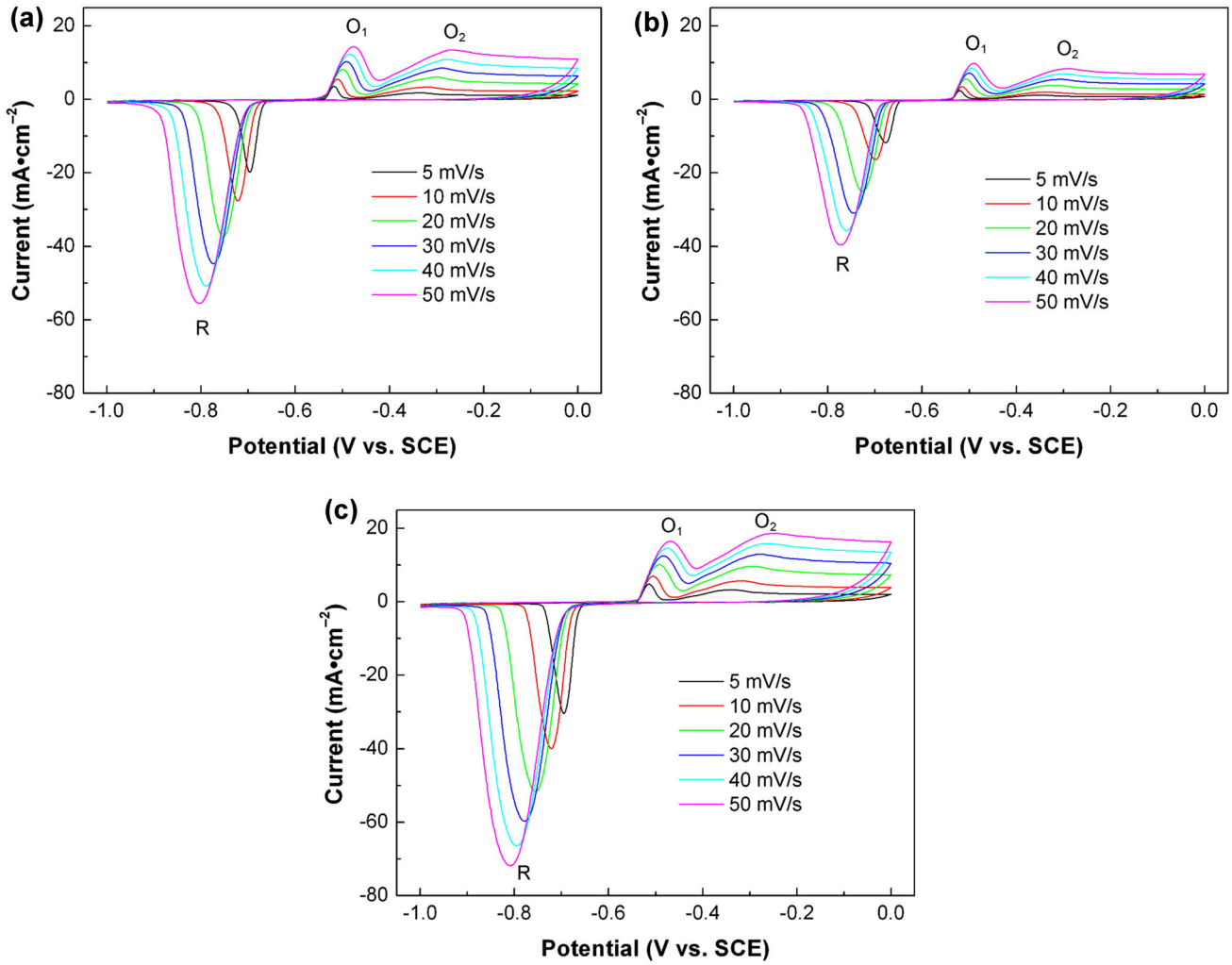

Fig. 2. CV curves of Bi_2WO_6 samples at various scan rates ranging from 5 mV s^{-1} to 50 mV s^{-1} over the potential window between −1.0 V and 0 V: (a) S-pH1, (b) S-pH7, (c) S-pH11.

S-pH1, S-pH7, and S-pH11 was obtained as 255 F g^{-1}, 214 F g^{-1}, and 412 F g^{-1}, respectively. With increase in the current density, the specific capacitance exhibited a decreasing trend. When the current density was raised up to 5 mA cm^{-2}, the specific capacitance decreased to 89 F g^{-1}, 69 F g^{-1}, and 143 F g^{-1} for the three samples, respectively. This could be due to an increase in ionic resistivity and a decrease in charge diffusion to inner active sites and the redox reaction rate.[29] Among the three types of morphology, the spherical structures delivered relatively higher specific capacitance. A possible reason for this is that the spherical particles had small size and good dispersibility, which is expected to improve their performance as supercapacitor electrodes.

The electrochemical cycling stability of the Bi_2WO_6 samples was evaluated by repeated charge–discharge measurements at constant current density of 3 mA cm^{-2}. Figure 4 shows the capacitance retention as a function of charge–discharge cycling number. The initial discharge capacitance of samples S-pH1, S-pH7, and S-pH11 was observed to be 121 F g^{-1}, 102 F g^{-1}, and 184 F g^{-1}, respectively. After 850 cycles, the capacitance of the three samples was found to be 105 F g^{-1}, 80 F g^{-1}, and 175 F g^{-1}, maintaining 87%, 78%, and 95% of the initial capacitance, respectively. Among the three types of Bi_2WO_6 morphology (flower-like hierarchical structures, flake-like structures, and spherical structures), the spherical structures exhibited the best cycling stability.

EIS measurements were carried out using a sinusoidal voltage pulse with amplitude of 5 mV in the frequency range from 1 Hz to 10^5 Hz. Figure 5 shows the Nyquist spectra obtained for the Bi_2WO_6 samples, and the inset shows the enlarged high-frequency region of the spectra. It is seen that the Nyquist spectra consist of a small semicircle in the high-frequency region, followed by a straight line in the low-frequency region. The semicircle is related

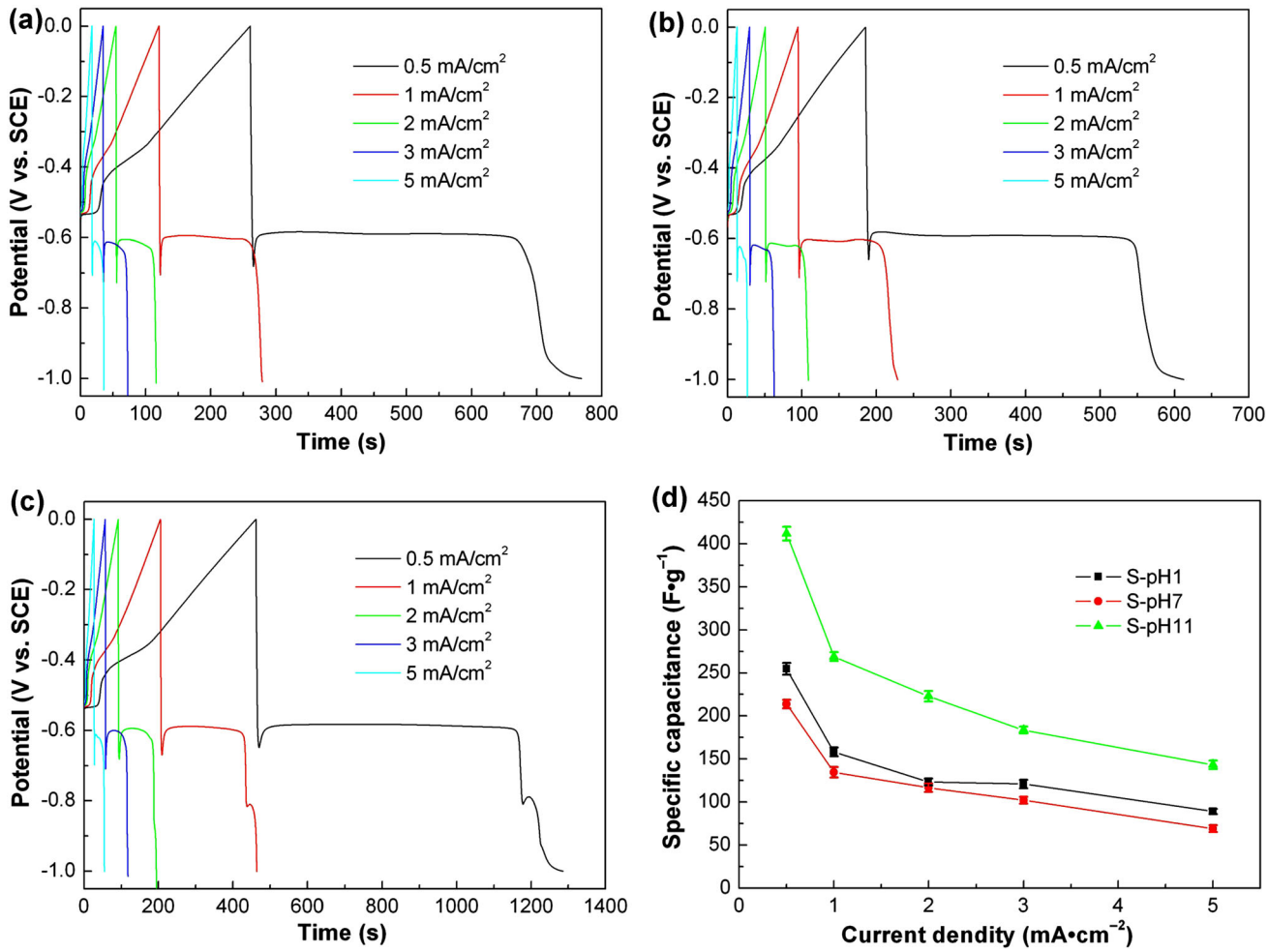

Fig. 3. Charge–discharge curves of samples (a) S-pH1, (b) S-pH7, and (c) S-pH11. (d) Calculated specific capacitance values of Bi_2WO_6 samples at various current densities.

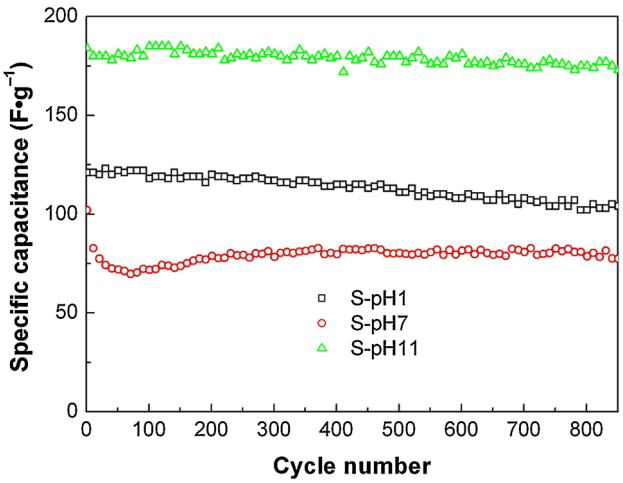

Fig. 4. Capacitance retention of Bi_2WO_6 samples as function of charge–discharge cycling number at constant current density of 3 mA cm^{-2}.

to the charge-transfer resistance at the electrode–electrolyte interface (i.e., Faradic resistance), whereas the straight line is ascribed to diffusion of the electrolyte ions into/from electrode pores.[30] The small semicircle observed in the Nyquist spectra for the Bi_2WO_6 samples indicates that the charge-transfer resistance is very small. Small charge-transfer resistance suggests that the Faradic reaction proceeds easily with high reversibility. The straight line in the Nyquist spectra reveals a phase angle above 45°, suggesting an important capacitive behavior for the Bi_2WO_6 samples. The EIS data could be fit by using the equivalent circuit shown in Fig. 5, which includes the solution resistance (R_s), double-layer capacitance (C_d), charge-transfer resistance (R_{ct}), and Warburg impedance (W). The first intersection point of the Nyquist spectra with the real axis corresponds to the solution resistance R_s, which is obtained as 0.91 Ω, 0.85 Ω, and 0.97 Ω for samples S-pH1, S-pH7, and S-pH11, respectively. The charge-transfer resistance R_{ct} is obtained by intercepting the semicircle with the real axis as 1.18 Ω, 1.19 Ω, and 0.91 Ω for the three samples, respectively. The double-layer capacitance C_d of the three samples was calculated to be 2.5×10^{-6} F, 2.1×10^{-6} F, and 2.8×10^{-6} F, respectively.

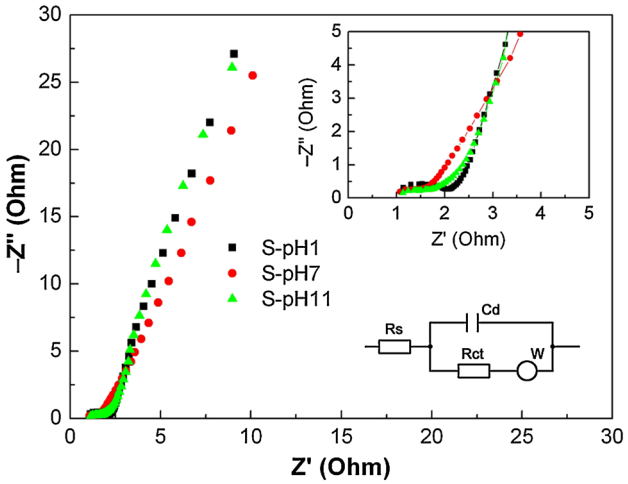

Fig. 5. Nyquist spectra of Bi_2WO_6 samples, with insets showing the enlarged high-frequency region of the spectra and the equivalent circuit.

CONCLUSIONS

Based on a hydrothermal route, Bi_2WO_6 with flower-like hierarchical, flake-like, and spherical structure was synthesized at pH 1, 7, and 11, respectively. The results of electrochemical tests revealed that the three Bi_2WO_6 samples exhibited pseudocapacitive behavior with specific capacitance of 255 F g^{-1}, 214 F g^{-1}, and 412 F g^{-1}, respectively, in 1 M KOH electrolyte at current density of 0.5 mA cm^{-2}. Evaluation of the electrochemical stability of the three samples at current density of 3 mA cm^{-2} revealed that their capacitance maintained 87%, 78%, and 95% of the initial value after 850 charge–discharge cycles, respectively. Compared with the flower-like hierarchical and flake-like structures, Bi_2WO_6 with spherical structure delivered relatively better electrochemical performance.

ACKNOWLEDGEMENTS

This work was supported by the National Natural Science Foundation of China (Grant No. 51262018), the Fundamental Research Funds for Universities of Gansu Province (Grant No. 056003), and the Hongliu Outstanding Talents Foundation of Lanzhou University of Technology (Grant No. J201205).

REFERENCES

1. P. Simon and Y. Gogotsi, *Nat. Mater.* 7, 845 (2008).
2. M. Winter and R.J. Brodd, *Chem. Rev.* 104, 4245 (2004).
3. B.E. Conway, *Electrochemical Supercapacitors: Scientific Fundamentals and Technological Applications* (New York: Kluwer Academic/Plenum, 1999), p. 13.
4. G.P. Wang, L. Zhang, and J.J. Zhang, *Chem. Soc. Rev.* 41, 797 (2012).
5. C. Merlet, B. Rotenberg, P.A. Madden, P.-L. Taberna, P. Simon, Y. Gogotsi, and M. Salanne, *Nat. Mater.* 11, 306 (2012).
6. Y.-H. Hsu, C.-C. Lai, C.-L. Ho, and C.-T. Lo, *Electrochim. Acta* 127, 369 (2014).
7. C.C. Hu, K.H. Chang, M.C. Lin, and Y.T. Wu, *Nano Lett.* 6, 2690 (2006).
8. Z.N. Yu, B. Duong, D. Abbitt, and J. Thoma, *Adv. Mater.* 25, 3302 (2013).
9. S. Shivakumara, T.R. Penki, and N. Munichandraiah, *Mater. Lett.* 131, 100 (2014).
10. R. Tummala, R.K. Guduru, and P.S. Mohanty, *J. Power Sources* 209, 44 (2012).
11. J. Yang, T.B. Lan, J.D. Liu, Y.F. Song, and M.D. Wei, *Electrochim. Acta* 105, 489 (2013).
12. G.A. Babu, G. Ravi, T. Mahalingam, M. Kumaresavanji, and Y. Hayakawa, *Dalton Trans.* 44, 4485 (2015).
13. F.L. Zheng, G.R. Li, Y.N. Ou, Z.L. Wang, C.Y. Su, and Y.X. Tong, *Chem. Commun.* 46, 5021 (2010).
14. D.P. Dubal, G.S. Gund, C.D. Lokhande, and R. Holze, *Mater. Res. Bull.* 48, 923 (2013).
15. H.W. Newkirk, P. Quadflieg, J. Liebertz, and A. Kockel, *Ferroelectrics* 4, 51 (1972).
16. H. Takeda, J.S. Han, M. Nishida, T. Shiosaki, T. Hoshina, and T. Tsurumi, *Solid State Commun.* 150, 836 (2010).
17. V.I. Utkin, Y.E. Roginskaya, V.I. Voronkova, V.K. Yanovskii, B.S. Galyamov, and Y.N. Ventevtsev, *Phys. Status Solidi A* 59, 75 (1980).
18. D.J. Wang, Y.Z. Zhen, G.L. Xue, F. Fu, X.M. Liu, and D.S. Li, *J. Mater. Chem. C* 1, 4153 (2013).
19. M. Tachibana, *Solid State Commun.* 211, 1 (2015).
20. A. Kudo and S. Hijii, *Chem. Lett.* 10, 1103 (1999).
21. J.W. Tang, Z.J. Zou, and J.H. Ye, *Catal. Lett.* 92, 53 (2004).
22. V.D. Nithya, R. Kalai Selvan, D. Kalpana, L. Vasylechko, and C. Sanjeeviraja, *Electrochim. Acta* 109, 720 (2013).
23. Z.M. Cui, H. Yang, B. Wang, R.S. Li, and X.X. Wang, *Nanoscale Res. Lett.* 11, 190 (2016).
24. V. Vivier, A. Regis, G. Sagon, J.Y. Nedelec, L.T. Yu, and C. Cachet-Vivier, *Electrochim. Acta* 46, 907 (2001).
25. V.D. Nithya, B. Hanitha, S. Surendran, D. Kalpana, and R. Kalai Selvan, *Ultrason. Sonochem.* 22, 300 (2015).
26. Z. Khan, S. Bhattu, S. Haram, and D. Khushalani, *RSC Adv.* 4, 17378 (2014).
27. Y.C. Zhang, H. Yang, W.P. Wang, H.M. Zhang, R.S. Li, X.X. Wang, and R.C. Yu, *J. Alloys Compd.* 684, 707 (2016).
28. V. Vivier, C. Cachet-Vivier, S. Mezaille, B.L. Wu, C.S. Cha, J.Y. Nedelec, M. Fedoroff, D. Michel, and L.T. Yu, *J. Electrochem. Soc.* 147, 4252 (2000).
29. M. Aghazadeh, A.N. Golikand, and M. Ghaemi, *Int. J. Hydrogen Energy* 36, 8674 (2011).
30. M.D. Stoller, S.J. Park, Y.W. Zhu, J.H. An, and R.S. Ruoff, *Nano Lett.* 8, 3498 (2008).